

# QUIJOTE scientific results – I. Measurements of the intensity and polarisation of the anomalous microwave emission in the Perseus molecular complex

R. Génova-Santos,<sup>1,2</sup>★ J. A. Rubiño Martín,<sup>1,2</sup> R. Rebolo,<sup>1,2,3</sup> A. Peláez-Santos,<sup>1,2</sup> C. H. López-Caraballo,<sup>1,2,4</sup> S. Harper,<sup>5</sup> R. A. Watson,<sup>5</sup> M. Ashdown,<sup>6,7</sup> R. B. Barreiro,<sup>8</sup> B. Casaponsa,<sup>8</sup> C. Dickinson,<sup>5</sup> J. M. Diego,<sup>8</sup> R. Fernández-Cobos,<sup>8</sup> K. J. B. Grainge,<sup>5,6</sup> C. M. Gutiérrez,<sup>1,2</sup> D. Herranz,<sup>8</sup> R. Hoyland,<sup>1</sup> A. Lasenby,<sup>6,7</sup> M. López-Caniego,<sup>8</sup> E. Martínez-González,<sup>8</sup> M. McCulloch,<sup>5</sup> S. Melhuish,<sup>5</sup> L. Piccirillo,<sup>5</sup> Y. C. Perrott,<sup>6</sup> F. Poidevin,<sup>1,2</sup> N. Razavi-Ghods,<sup>6</sup> P. F. Scott,<sup>6</sup> D. Titterington,<sup>6</sup> D. Tramonte,<sup>1,2</sup> P. Vielva<sup>8</sup> and R. Vignaga<sup>1,2</sup>

<sup>1</sup>Instituto de Astrofísica de Canarias, 38200 La Laguna, E-38200 Tenerife, Canary Islands, Spain

<sup>2</sup>Departamento de Astrofísica, Universidad de La Laguna (ULL), E-38206 La Laguna, Tenerife, Spain

<sup>3</sup>Consejo Superior de Investigaciones Científicas, Madrid, Spain

<sup>4</sup>Departamento de Física y Astronomía, Universidad de la Serena, Av. Cisternas 1200, 1720236 La Serena, Chile

<sup>5</sup>Jodrell Bank Centre for Astrophysics, Alan Turing Building, School of Physics and Astronomy, The University of Manchester, Oxford Road, Manchester M13 9PL, UK

<sup>6</sup>Astrophysics Group, Cavendish Laboratory, University of Cambridge, J.J. Thomson Avenue, Cambridge CB3 0HE, UK

<sup>7</sup>Kavli Institute for Cosmology, Madingley Road, Cambridge CB3 0HA, UK

<sup>8</sup>Instituto de Física de Cantabria (CSIC-Universidad de Cantabria), Avda. de los Castros s/n, E-39005 Santander, Spain

Accepted 2015 June 23. Received 2015 June 11; in original form 2014 December 23

## ABSTRACT

In this paper, we present Q-U-I JOint Tenerife Experiment (QUIJOTE) 10–20 GHz observations (194 h in total over  $\approx 250 \text{ deg}^2$ ) in intensity and polarisation of G159.6-18.5, one of the most widely studied regions harbouring anomalous microwave emission (AME). By combining with other publicly available intensity data, we achieve the most precise spectrum of the AME measured to date in an individual region, with 13 independent data points between 10 and 50 GHz being dominated by this emission. The four QUIJOTE data points provide the first independent confirmation of the downturn of the AME spectrum at low frequencies, initially unveiled by the COSMOlogical Structures On Medium Angular Scales experiment in this region. Our polarisation maps, which have an angular resolution of  $\approx 1^\circ$  and a sensitivity of  $\approx 25 \mu\text{K beam}^{-1}$ , are consistent with zero polarisation. We obtain upper limits on the polarisation fraction of  $\Pi < 6.3$  and  $< 2.8$  per cent (95 per cent C.L.), respectively, at 12 and 18 GHz ( $\Pi_{\text{AME}} < 10.1$  and  $< 3.4$  per cent with respect to the residual AME intensity), a frequency range where no AME polarisation observations have been reported to date. The combination of these constraints with those from other experiments confirm that all the magnetic dust models based on single-domain grains, and most of those considering randomly oriented magnetic inclusions, predict higher polarisation levels than is observed towards regions with AME. Also, neither of the two considered models of electric dipole emission seems to be compatible with all the observations together. More stringent constraints of the AME polarisation at 10–40 GHz are necessary to disentangle between different models, to which future QUIJOTE data will contribute.

**Key words:** radiation mechanisms: general – ISM: individual objects: G159.6-18.5 – diffuse radiation – radio continuum: ISM.

\* E-mail: rgs@iac.es

## 1 INTRODUCTION

The study of Galactic foregrounds is important not only to improve our knowledge of the physics of the interstellar medium (ISM) but to characterize the contamination that hinder the extraction of the cosmological signal from the cosmic microwave background (CMB) radiation. Now that several experiments are starting to search for the primordial B-mode anisotropy from inflation in the CMB polarisation (Kamionkowski, Kosowsky & Stebbins 1997; Zaldarriaga & Seljak 1997), having an accurate characterization of the polarisation of the foreground emission is becoming increasingly important. The *Planck* collaboration has recently released full-sky polarisation maps at frequencies up to 353 GHz that will allow to characterize the polarisation level of the thermal dust emission. Experiments operating in the microwave range, like Q-U-I JOint Tenerife Experiment (QUIJOTE; Rubiño-Martín et al. 2012a), will provide information about the polarisation of the synchrotron radiation. In total intensity, free-free emission and the so-called anomalous microwave emission (AME) also show up in this frequency range. While the former is known to be practically unpolarized (Rybicki & Lightman 1979), very little is known about the polarisation level of the AME.

Since its discovery in the 90s (Kogut et al. 1996a,b; Leitch et al. 1997), many observations in large-sky areas (de Oliveira-Costa et al. 1998, 1999; Davies et al. 2006) and in individual Galactic (Finkbeiner et al. 2002; Watson et al. 2005; Casassus et al. 2006; Dickinson et al. 2009; AMI Consortium et al. 2009; Tibbs et al. 2010; Génova-Santos et al. 2011; Vidal et al. 2011; Planck Collaboration XX 2011; Planck Collaboration XV 2014a; Battistelli et al. 2015) and extragalactic (Murphy et al. 2010) clouds have contributed to the understanding of the physical properties of this emission. A great deal of effort has also been dedicated to theoretical modelling of AME. Electric dipole radiation from very small and rapidly rotating dust grains in the ISM (Draine & Lazarian 1998; Ali-Haïmoud, Hirata & Dickinson 2009; Hoang, Draine & Lazarian 2010; Ysard & Verstraete 2010; Silsbee, Ali-Haïmoud & Hirata 2011), the so-called *spinning dust emission*, is the scenario that best fits the observations. An alternative mechanism based on magnetic dipole emission has also been proposed (Draine & Lazarian 1999; Draine & Hensley 2013), with a spectrum peaking at higher frequencies.

There are also some theoretical studies of the AME polarisation in the literature. After the first predictions by Lazarian & Draine (2000) of spinning dust polarisation, more recently Hoang, Lazarian & Martin (2013) presented a model based on observations of the UV polarisation bump, according to which the maximum polarisation fraction would be  $\approx 3$  per cent, at a frequency of 5 GHz. In regard to the magnetic dipole emission model, while Draine & Lazarian (1999) predicted high polarisation fractions (up to 40 per cent) in the case of dust grains with atomic magnetic moments oriented in a single domain, Draine & Hensley (2013) recently presented a more realistic model, with randomly oriented magnetic inclusions, which results in lower polarisation degrees ( $\lesssim 5$  per cent in the range 10–20 GHz). However, not much is known, from the observational standpoint, about the polarisation properties of the AME. Using *Wilkinson Microwave Anisotropy Probe* (WMAP) 5 yr data Macellari et al. (2011) set an upper limit  $\Pi < 5$  per cent (this and other upper limits that will be referred to in this section are at the 95 per cent confidence level) on the polarisation fraction of the diffuse AME. Some other constraints refer to individual clouds. Battistelli et al. (2006) observed the Perseus molecular complex with the COSMOlogical Structures On Medium Angular Scales (COSMOSOMAS) experiment and derived  $\Pi = 3.4^{+1.5}_{-1.9}$  per cent at 11 GHz.

Casassus et al. (2008) reported an upper limit of  $< 1.0$  per cent at 31 GHz on the  $\rho$  Ophiuchi molecular cloud using the *Cosmic Background Imager*, whereas Mason et al. (2009) found a maximum of  $< 2.7$  per cent with the Green Bank Telescope (GBT) at 9 GHz. More recently, López-Caraballo et al. (2011) obtained an upper limit of  $< 1.0$  per cent at 23 GHz on the Perseus molecular complex using *WMAP* 7 yr data. Shortly after this paper Dickinson, Peel & Vidal (2011), using the same data, obtained  $< 1.4$  per cent in the same region, and  $< 1.7$  per cent in  $\rho$  Ophiuchi. A detailed review of all these observations, plus some updated constraints in some regions, has been presented in Rubiño-Martín et al. (2012b).

In this paper, we present the first results obtained with the QUIJOTE experiment, that are based on observations of G159.6-18.5 in the Perseus molecular complex, one of the most studied AME regions in the sky (Watson et al. 2005; Tibbs et al. 2010, 2013; Planck Collaboration XX 2011; Planck Collaboration XV 2014a). QUIJOTE observations cover the frequency range 10–20 GHz, where only the COSMOSOMAS experiment had provided observations of the AME before. The goal of this paper is twofold: to confirm the downturn of the AME spectrum at frequencies below 23 GHz through similar spectral sampling but completely independent results to those provided by COSMOSOMAS, and to set constraints on the polarisation level of the AME in the so far unexplored spectral region between 12 and 20 GHz. Section 2 is dedicated to the description of the observations and the basics of the data reduction. Our main results are presented in Section 3, while the conclusions of this work are discussed in Section 4.

## 2 DATA AND METHODOLOGY

### 2.1 QUIJOTE data

The new data presented in this paper were acquired with the QUIJOTE experiment. QUIJOTE is a collaborative project that consists of two telescopes and three polarimeter instruments covering, respectively, the frequencies 10–20, 30 and 40 GHz, and located at the Teide Observatory (2400 m a.s.l.) in Tenerife (Spain). The main science driver of this experiment is to perform observations of the CMB polarisation to constrain the B-mode signal down to  $r = 0.05$ . A secondary goal is to characterize the polarisation of low-frequency foregrounds, mainly synchrotron emission and the AME, so that this signal can be removed from the primordial maps to a level appropriate for the desired level of  $r$ . The two QUIJOTE telescopes are based on an offset crossed-Dragone design, with projected apertures of 2.25 and 1.89 m for the primary and secondary mirrors, and provide highly symmetric beams (ellipticity  $> 0.98$ ) with very low sidelobes ( $\leq -40$  dB) and polarisation leakage ( $\leq -25$  dB). The first instrument to be fielded on the first QUIJOTE telescope is a multifrequency instrument (MFI) with four horns covering the frequency range 10–20 GHz, and with angular resolutions close to  $1^\circ$ . These detectors are fitted with MMIC low-noise amplifiers (noise temperature better than 10 K), and use stepped polar modulators to measure the polarisation of the incoming radiation, providing instantaneous sensitivities of  $\approx 650 \mu\text{K s}^{1/2}$  in four individual bands with nominal frequencies: 11, 13, 17 and 19 GHz. The median integrated PWV above the observatory is  $\approx 4$  mm, giving a zenith atmospheric temperature of  $\approx 2$  K at 11 GHz and  $\approx 5$  K at 19 GHz. The MFI saw first light on 2012 November and since then it has been performing routine observations of different Galactic and cosmological regions. The second instrument consists of 31 polarimeters at 30 GHz (TGI, thirty-gigahertz instrument), and is based on the same design of the MFI except that the polarisation modulation

is achieved electronically through phase switches. This instrument will be commissioned during 2015. Finally, the third instrument is planned to have 31 polarimeters at 40 GHz (FGI, forty-gigahertz instrument). Using the TGI and the FGI, which will provide instantaneous sensitivities of  $50 \mu\text{K s}^{1/2}$ , we plan to survey an area of  $3000 \text{ deg}^2$  down to a projected sensitivity of  $\leq 1 \mu\text{K beam}^{-1}$ . A more detailed description of the technical and scientific aspects of this project can be found in Rubiño-Martín et al. (2012a) or in Rebolo et al. (in preparation).

### 2.1.1 Observations

The observations covering the Perseus molecular complex were carried out between 2012 December and 2013 April using the MFI, in four frequency bands centred at 11.2, 12.9, 16.7 and 18.7 GHz. The beam FWHMs are 0.87, for the two lower frequencies, and 0.65, for the two high-frequency bands. The observations consisted of raster scans at constant elevation in order to minimize the effect of atmospheric variations. Each scan had an amplitude in azimuth direction of 12 degrees centred around the coordinates RA =  $3^{\text{h}}52^{\text{m}}$ , Dec. =  $34^{\circ}$ . This position was chosen to be equidistant between the AME cloud G159.6-18.5 and the California H II region (NGC 1499), which is also observed in the scans and is used as a null test for zero polarisation. In each raster scan, of total integration time of 30–35 min, the telescope moves back and forth in azimuth at a velocity of  $1^{\circ} \text{ s}^{-1}$ . A total of 336 raster scans were performed, in four positions of the polar modulators ( $0^{\circ}, 22.5^{\circ}, 45^{\circ}$  and  $67.5^{\circ}$ ) in order to minimize systematics. In total 194.4 h of data were accumulated, 23 per cent of which were removed due to being affected by bad weather or instrumental effects, resulting in a final effective observing time of 148.9 h.

The analyses that will be presented in this paper were carried out using data from only two horns of the MFI. Data from the other two were ignored because of the uncertainty in the determination of the modulator angle (horn 1) and higher noise of the amplifiers (horn 4).<sup>1</sup> As the MFI horns are separated typically by  $5^{\circ}$  on the sky, the sky coverage of each one is different. The total sky area covered by the two horns used here was, respectively, 184 and  $277 \text{ deg}^2$ .

### 2.1.2 Amplitude calibration

We determine the gain calibration factors (giving the conversion from voltage measured in the detectors to temperature on the sky) using total intensity measurements on Cas A, which is ideal as it is bright and has a very low degree of polarisation. We do daily 25 min raster scans of  $10^{\circ} \times 10^{\circ}$  around this source from which we derive the gain calibration factors for each channel. The output signal of each channel is a combination of the three Stokes parameters  $I$ ,  $Q$  and  $U$ . According to WMAP the polarized flux density of Cas A at 22.8 GHz is  $P = 0.81 \pm 0.05 \text{ Jy}$  (polarisation fraction  $\Pi = 0.35 \pm 0.02$  per cent; Weiland et al. 2011), which is low enough not to be detected in a single raster scan. We can therefore safely assume  $Q = U = 0$ , and use the  $I$  flux density to calibrate. To achieve this, we use the modelled spectrum of Weiland et al. (2011), which is obtained by fitting a combination of WMAP 7 yr data and other ancillary data to a logarithmic quadratic function. This function is then integrated over the measured spectral transmission

of each frequency band to obtain the reference Cas A flux densities associated with each channel.

Finally, as the previous model is referred to epoch 2000, in order to account for the secular decrease of the Cas A flux density (typically 0.5 per cent  $\text{yr}^{-1}$ ), we use the Hafez et al. (2008) model, which was derived using Very Small Array observations, in order to refer the final flux densities to the time of the observations. In order to circumvent possible uncertainties associated with this secular variation, a more suitable calibration source would be Jupiter. However, owing to its small angular size, this source is severely diluted in the QUIJOTE beams and a large number of observations would be required for it to be used as primary calibrator. We point out that, in any case, the gain calibration will only affect the modelling of the spectral energy distribution (SED) in G159.6-18.5. The gain calibration factors will cancel out when dividing the polarized intensity by the total intensity, and therefore the inferred polarisation fractions, which are one of the main goals of this paper, are insensitive to the absolute flux calibration.

### 2.1.3 Polarisation calibration

One of the main steps of the data processing is the calibration of the polarisation angle  $\varphi_0$ , which is defined as the reference position angle of each polar modulator. To accomplish this, we use Tau A (also known as the Crab nebula) as a calibrator, which is the brightest polarized source in the sky in the microwave range. We perform daily 25 min raster scans of  $10^{\circ} \times 10^{\circ}$  around this source, from which we derive a polarized flux that is a function of the intrinsic  $Q/I$  and  $U/I$ , of the position of the modulator relative to  $\varphi_0$  and of the parallactic angle  $\varphi_p$ . WMAP 7 yr results (Weiland et al. 2011) show that the  $Q/I$  and  $U/I$  ratios for Tau A do not significantly vary (less than 2 per cent, which is consistent with the error of the measurement) between 23 and 94 GHz. We therefore assume that these factors will remain equally unchanged down to 10 GHz, and use as reference the WMAP measurements at 22.8 GHz, the closest frequency. As we also know  $\varphi_p$ , we can therefore fit for  $\varphi_0$ .

Using 191 raster scans on Tau A throughout a year, we have checked that the recovered polarisation angle,  $\varphi_0$ , is stable over time. We then combine all these observations to derive a unique value for each horn. The accuracy on the determination of this angle is, respectively,  $0.8^{\circ}$  and  $0.4^{\circ}$  for the two horns that will be used in the polarisation analyses that will be presented in this paper. In QUIET, an experiment which has similarities with QUIJOTE, a precision of  $0.5^{\circ}$  is achieved by using a combination of Tau A observations with a sparse-wire-grid calibrator (QUIET Collaboration 2012). We point out however that the accurate determination of this angle is important only to derive precise  $Q$  and  $U$  flux densities. An incorrect angle will result in a mixing of flux between  $Q$  and  $U$ , but the polarized intensity  $P = \sqrt{Q^2 + U^2}$  will remain unchanged. As in this analysis we will get constraints on the polarisation fraction, the accurate calibration of the polarisation angle is unimportant.

### 2.1.4 Map making

The four output channels of each frequency band contain a combination of three Stokes parameters  $I$ ,  $Q$  and  $U$ . The sum of these channels, after calibration of their individual gains, gives  $I$ , while the subtraction of pairs of channels gives the following combination of  $Q$  and  $U$ :

$$V_{\text{sub}} = Q \sin(4\varphi_{\text{pm}} + 2\varphi_p) + U \cos(4\varphi_{\text{pm}} + 2\varphi_p), \quad (1)$$

<sup>1</sup> The amplifiers of this horn have now been replaced, providing a higher sensitivity than before.

where  $\varphi_{\text{pm}}$  is the position angle of the polar modulator, whose reference position is calibrated following the procedure explained in Section 2.1.3, and  $\varphi_p$  is the parallactic angle. Out of the four channels, two are correlated and therefore are affected by the same  $1/f$  noise, while the two other are not. To reconstruct the polarisation signal, we then only use the two correlated channels, in order to minimize the  $1/f$  contribution. The typical knee frequencies of our receivers are  $f_k \sim 10\text{--}40$  Hz depending on the channel. However, for the measurement of polarisation, the subtraction results in much lower values of  $f_k \sim 0.1\text{--}0.2$  Hz. In order to further reduce the  $1/f$  noise in the final maps, we apply a filter on the time-ordered-data (TOD) by subtracting the median of the data in intervals of 20 s, after binning the data at 50 ms.

Under the assumption that the filtered TODs are dominated by white noise, we consider the noise covariance matrix to be diagonal, a hypothesis that considerably simplifies the map making. As the response of our instrument to polarisation is a combination of  $Q$  and  $U$ , in order to recover these Stokes parameters in each pixel we have to combine all the samples lying in that pixel corresponding to different angles  $\varphi = 4\varphi_{\text{pm}} + 2\varphi_p$ . To do so we use two independent strategies. The first one consists in producing 100 maps, each one corresponding to  $\varphi$  angles within a given bin, and then using the 100 values of each pixel to find the best-fitting solution for  $Q$  and  $U$  from equation (1). The second strategy builds on an analytical  $\chi^2$  minimization. The different parameters, which are combinations of sines and cosines of the  $\varphi$  angles, are grouped in each pixel, and at the end of the process the  $Q$  and  $U$  values are computed using the analytical formulae that result from this minimization. In both cases, the data samples are weighted according to their noise, which is calculated from the standard deviation calculated during the binning of the TODs.

To produce the final maps, we use a HEALPix pixelization (Górski et al. 2005) with  $N_{\text{side}} = 512$  (pixel size 6.9 arcmin), which is sufficient given the beam FWHM. While we have checked that the maps resulting from the two strategies are almost identical, in the subsequent analyses we use those resulting from the second method, since it is considered to be more accurate as it does not require a discretization of the  $\varphi$  angles.

## 2.2 Ancillary data

All the polarisation data that will be used in this paper come from the QUIJOTE experiment. However, in order to obtain the full SED of G159.6-18.5, from which the residual AME fluxes will be inferred, we use ancillary data from other experiments. In the low-frequency range, we use the Haslam et al. (1982) map<sup>2</sup> at 0.408, the Berkhuijsen (1972) map<sup>3</sup> at 0.820 and the Reich & Reich (1986) map at 1.4 GHz.

At 10.9, 12.7, 14.7 and 16.3 GHz, similar frequencies to QUIJOTE, we use data from the COSMOSMAS experiment (Watson et al. 2005). In order to minimize the  $1/f$  noise, the data from this experiment were filtered by the suppression of the first seven harmonics in the FFT of the circular scans, which results in a flux loss on large angular scales. For this reason, the comparison with other experiments that preserve all the angular scales is not straightforward. It is necessary to account for the flux lost, as it was done in Planck Collaboration XX (2011). The fluxes presented in that paper are already corrected, so we directly take those fluxes.

<sup>2</sup> We use the map supplied by Platania et al. (2003).

<sup>3</sup> We projected the map downloaded from <http://www.mpifr-bonn.mpg.de/survey.html> into HEALPix pixelization.

We also use data from the 9 yr release of the WMAP satellite<sup>4</sup> (Bennett et al. 2013) to provide flux density estimates at frequencies 23, 33, 41, 61 and 94 GHz. Recent data from the first release of the *Planck* mission<sup>5</sup> (Planck Collaboration I 2014b) cover the frequencies 28, 44, 70, 100, 143, 217, 353, 545 and 857 GHz. We also download the released Type 1 CO maps (Planck Collaboration XIII 2014d), which are used to correct the 100, 217 and 353 GHz frequency maps from the contamination introduced by the CO rotational transition lines (1–0), (2–1) and (3–2), respectively. Finally, in the far-infrared spectral range we use Zodi-Subtracted Mission Average COsmic Background Explorer-Diffuse InfraRed Background Experiment maps (Hauser et al. 1998) at 240 (1249 GHz), 140 (2141 GHz) and 100  $\mu\text{m}$  (2998 GHz).

## 2.3 Methodology for flux estimation

Intensity and polarisation fluxes will be calculated by applying an aperture photometry integration on the maps. This is a well known and widely used technique in this context (López-Caraballo et al. 2011; Dickinson et al. 2011; Génova-Santos et al. 2011), consisting of integrating temperatures of all pixels within a given aperture, and subtracting a background level calculated in an external ring. Instead of the mean, following Planck Collaboration XX (2011), we chose to use the median of all the pixels in the external ring as the estimate of the background level. The median is a better proxy for the real level in cases of strongly variable backgrounds with many outlier pixels. The flux density is then given by

$$S_v = a(v) \left[ \frac{\sum_{i=1}^{n_1} T_i}{n_1} - \bar{T}_j \right], \quad (2)$$

where  $n_1$  is the number of pixels in the aperture, and  $T_i$  and  $\bar{T}_j$  represent, respectively, the pixel thermodynamic temperatures in the aperture and in the background annulus. The median is calculated over the  $n_2$  pixels in this annulus. The function  $a(v)$  gives the conversion factor from temperature to flux density,

$$a(v) = \frac{h^2 v^4}{2k_b T_{\text{cmb}}^2 c^2} \sinh^{-2} \left( \frac{hv}{2k_b T_{\text{cmb}}} \right) n_1 \Omega_{\text{pix}}, \quad (3)$$

where  $h$  and  $k_b$  are the Planck and Boltzmann constants,  $c$  is the speed of light,  $T_{\text{cmb}} = 2.725$  K (Mather et al. 1999) is the CMB temperature and  $\Omega_{\text{pix}}$  is the solid angle subtended by each pixel.

The determination of the error associated with the previous estimate is crucial for the results of this paper. In a hypothetical case of perfect white uncorrelated noise, it could easily be estimated through:

$$\sigma(S_v) = a(v) \left[ \frac{\sum_{i=1}^{n_1} \sigma_i^2}{n_1^2} + \frac{\pi}{2} \frac{\sum_{i=1}^{n_2} \sigma_j^2}{n_2^2} \right]^{1/2}, \quad (4)$$

where  $\sigma$  represents the error of each pixel.

However, in QUIJOTE the instrument noise is correlated due to the presence of  $1/f$  residuals, and also the Galactic background fluctuations introduce, mainly in total intensity, an important contribution to the error which is correlated on the order of the beam size. Ideally, we should then use the covariance matrices of the instrument and background noises. The former can be extracted through a characterization of the  $1/f$  noise spectrum, however the

<sup>4</sup> Downloaded from the LAMBDA data base, <http://lambda.gsfc.nasa.gov/>

<sup>5</sup> Downloaded from the *Planck* Legacy Archive, <http://pla.esac.esa.int/pla/>

latter is difficult to determine. Instead, in the previous equation we can introduce in the denominator the number of independent pixels in the aperture and in the ring, which we will denote, respectively, as  $n'_1$  and  $n'_2$ . The pixel variance will be calculated from the pixel-to-pixel standard deviation of all the pixel temperatures  $T_j$  in the background,  $\sigma(T_j)$ . Obviously, the standard deviation of the pixels in the aperture would be biased by the presence of the source. On the contrary, the standard deviation of the pixels in the ring gives a reasonable estimate of the contributions of the background and of the instrumental noise to the true error. Therefore, the final equation that we will use to estimate errors in this paper reads as:

$$\sigma(S_v) = a(v)\sigma(T_j)\sqrt{\frac{1}{n'_1} + \frac{\pi}{2}\frac{1}{n'_2}}. \quad (5)$$

In the case of the error being completely dominated by the background, then we could use for  $n'_1$  and  $n'_2$  the number of beams in the aperture and in the background,  $n^b_1$  and  $n^b_2$ . However, while being particularly strong in intensity, the background fluctuations from the Galactic emission are not so important in polarisation. For this reason, in this case the relative contribution from the  $1/f$  residuals to the uncertainty is significant. To quantify this, we selected 20 random positions around our source, G159.6-18.5, and performed flux integration on those positions using the same aperture and ring sizes. The standard deviation of those values gives a reasonable estimation of the true noise of our flux density estimate. From this analysis, we determined that for total intensity  $n'_{1,2} = n^b_{1,2}$ , while for polarisation  $n'_{1,2} = 2n^b_{1,2}$ . This is what we will use in our estimation of the flux errors.

In cases of low signal-to-noise fluxes, or when placing upper limits on the polarized flux density  $P$ , as it will be our case, it is necessary to de-bias the fluxes derived from the aperture photometry integration. This requirement comes from the fact that the posterior distribution of the polarized intensity  $P$  does not follow a normal (Gaussian) distribution. Furthermore  $P$  is a quantity that must always be positive, and this introduces a bias into any estimate. For any true  $P_0$  we would expect to measure on average a polarisation  $P > P_0$ . In order to get the de-biased fluxes,  $P_{\text{db}}$ , from the measured ones,  $P$ , we choose the Bayesian approach described in Vaillancourt (2006) and in Rubiño-Martín et al. (2012b), consisting of integrating the analytical posterior probability density function over the parameter space of the true polarisation. The same posterior cannot be used for the polarisation fraction,  $\Pi = P/I \times 100$ , as it follows a different distribution. As, to our knowledge, there is not in the literature any analytical solution for the posterior distribution of  $\Pi$ , we numerically evaluate this function by applying Monte Carlo simulations. This approach has already been carried out in López-Caraballo et al. (2011) and in Dickinson et al. (2011).

### 3 RESULTS AND DISCUSSION

#### 3.1 Maps and consistency tests

In Fig. 1, we show the intensity map at 11 GHz resulting from combining 149 h of observations, where emissions from G159.6-18.5, the California nebula (NGC 1499) and the 3C84 quasar are clearly visible. More detailed  $I$ ,  $Q$  and  $U$  maps at our four frequencies around the position of G159.6-18.5 are shown in Fig. 2. The  $Q$  and  $U$  maps on this source are consistent with zero polarisation, and therefore upper limits on the polarized flux density will be extracted in Section 3.3. Some striping is clearly visible in the maps, which is produced by the presence of regions with a higher noise

due to a lower integration time per pixel and, to a lesser extent, to  $1/f$  residuals. The inhomogeneities in the coverage (integration time per pixel) maps are caused by the separation of the horns in the focal plane, which leads the sky coverage to be different when we observe the field before or after crossing the local meridian. In the  $Q$  and  $U$  maps at 11 and 13 GHz of Fig. 2, the two orthogonal stripes with clearly higher noise correspond to regions with integration of  $\sim 3\text{--}7$  s pixel $^{-1}$  (pixel size 6.9 arcmin). By comparison, in the central region inside the circle where we perform the aperture photometry, the integration time is  $\sim 30\text{--}35$  s pixel $^{-1}$ , resulting in a lower pixel-to-pixel dispersion of the data.

An important consistency test, that may reveal the presence of systematics and other spurious effects, is obtained through jackknife maps. We have uniformly split our full data set in two halves in such a way that the maps of number of hits associated to these two halves are as similar as possible. The differences of the two halves divided by two, for the intensity and polarisation maps at our four frequencies, are shown in Fig. 3. As expected, the intensity emission coming from G159.6-18.5 is consistently cancelled out in these maps. While a similar striping pattern to the maps in Fig. 2 is seen, these maps are dominated by instrumental noise. This is confirmed by the noise values shown in Table 1, where we compare the pixel-to-pixel rms calculated in two different regions: the external ring that we will use for background subtraction when calculating the intensity and polarisation flux densities, and a region of very low sky emission enclosed by the dashed circle represented in Fig. 3. The rms values in  $Q$  and  $U$  are similar in the original maps and in the sum and difference of the two halves. They are typically  $\sim 250 \mu\text{K} \text{ pixel}^{-1}$  (pixel size: 6.9 arcmin) or  $\sim 25 \mu\text{K} \text{ beam}^{-1}$  (beam size: 1  $\sim$  degree). In the case of the  $I$  maps, the rms in the background ring are higher in the sum than in the difference because of the emission of the source. In the circle with low sky signal the values in the sum and in the difference maps are very similar.

The last column of Table 1 shows the average rms levels in the  $Q$  and  $U$  maps normalized by the integration time per pixel. As the number of hits per pixel is very inhomogeneous, to calculate these numbers we have made a realization of Gaussian noise in which we assign to each pixel a noise proportional to  $t_{\text{pix}}^{-1/2}$ , where  $t_{\text{pix}}$  is the integration time per pixel, and then calculate the pixel-to-pixel rms. The amplitudes of the white noise in the spectra of the TOD range between 898 (at 16.7 GHz) and 1228  $\mu\text{K s}^{1/2}$  (at 11.2 GHz).<sup>6</sup>  $1/f$  residuals make the noises calculated on the maps only slightly higher, typically by a factor  $\sim 15$  per cent, confirming our previous statement that these maps are dominated by white (Gaussian) noise.

Another important consistency test for the presence of systematics, and in particular for the  $I$  to  $Q/U$  polarisation leakage, is to confirm that our polarisation maps are consistent with noise in the position of unpolarized sources. This verification is provided by the nearby California H II region, which is also covered by our observations. As any standard H II region, it is dominated by free-free emission at the QUIJOTE frequencies, which is known to be practically unpolarized. In Fig. 4, we show intensity and polarisation maps towards the California region, showing that the  $Q$  and  $U$  maps are consistent with zero polarisation.

<sup>6</sup> Note that in this paper we are using data from only two out of the four horns of QUIJOTE. If all four horns were used, then the global sensitivities of the experiment are a factor  $\sqrt{2}$  better, i.e.  $\approx 650 \mu\text{K s}^{1/2}$ , the number quoted in Section 2.1.

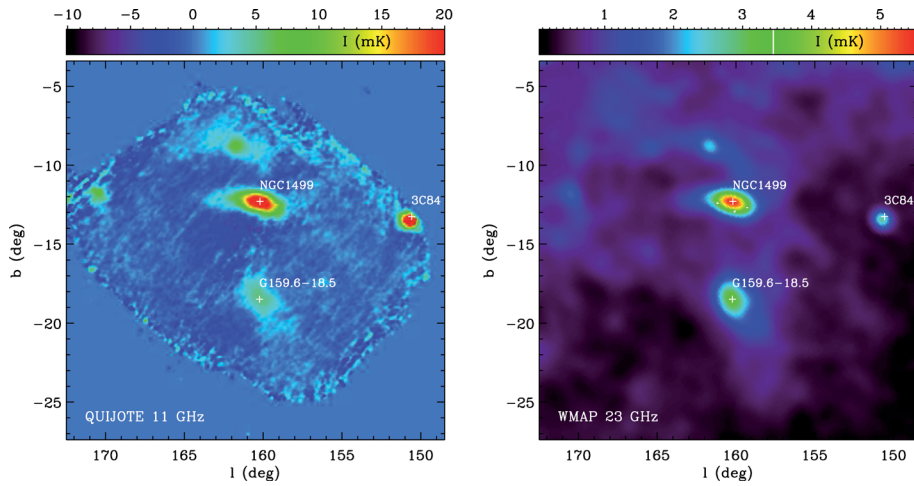


**Figure 1.** QUIJOTE intensity map at 11 GHz of the whole region covered by the observations (left), in comparison with the WMAP 9 yr map at 23 GHz (right). The positions of the G159.6-18.5 molecular cloud, the California H II region (NGC 1499) and the 3C84 quasar are marked with crosses. The QUIJOTE map encompasses  $277 \text{ deg}^2$ , contains in total 149 h of observations, and its rms is  $\approx 80 \mu\text{K beam}^{-1}$ . By comparing the relative amplitudes of California and G159.6-18.5, it can easily be noted how the presence of AME boosts the brightness of G159.6-18.5 at 23 GHz.

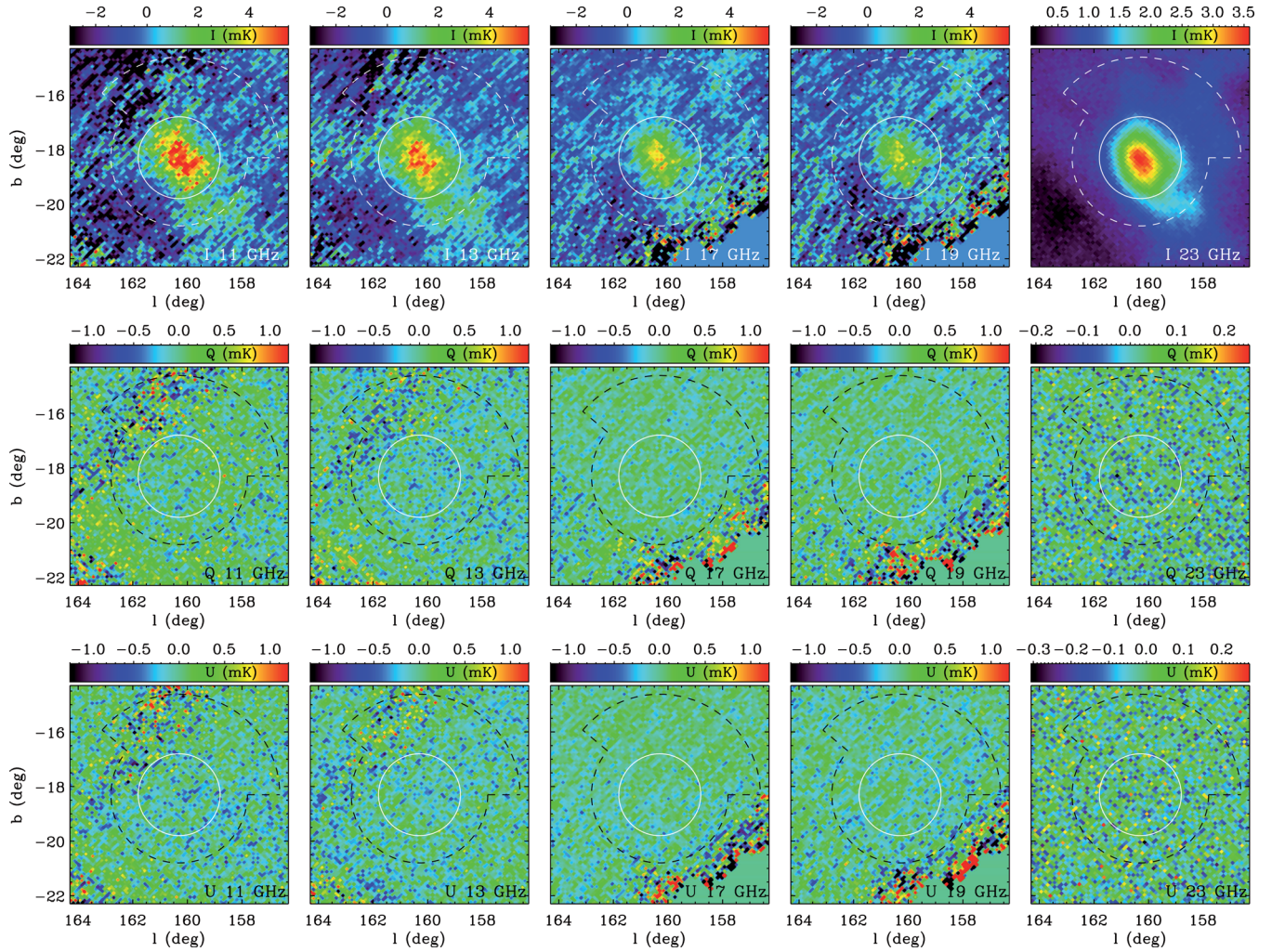


**Figure 2.** Intensity and polarisation maps at the QUIJOTE four frequency channels around the G159.6-18.5 molecular cloud. The Stokes  $Q$  and  $U$  maps show zero polarisation. The solid circle shows the aperture we use for flux integration, whereas the dashed contour limits the extent of the ring we use for background subtraction. For comparison, in the last column we plot the corresponding WMAP 9 yr maps at 23 GHz.

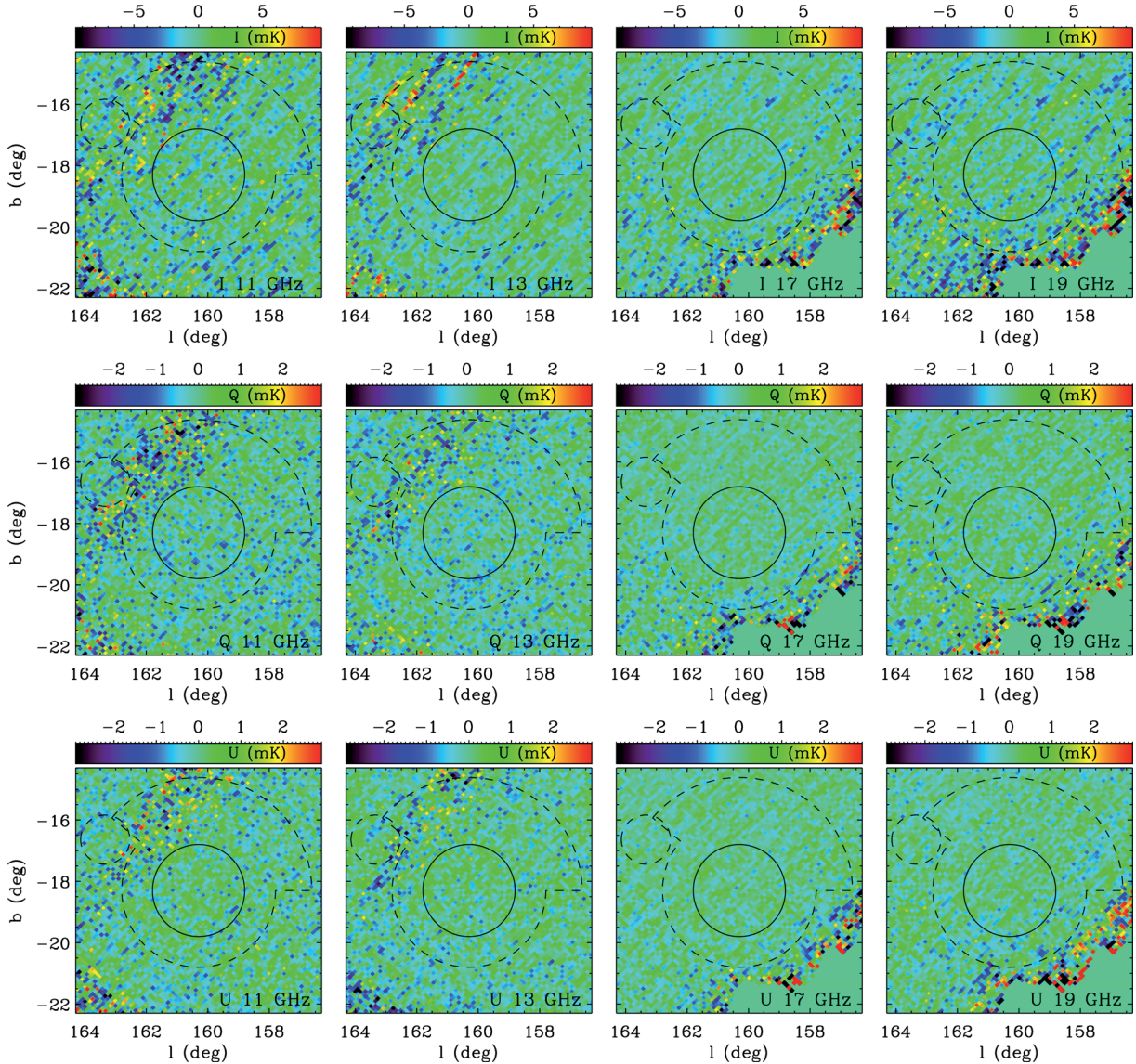


**Figure 3.** Jackknife difference maps at the four frequencies around the G159.6-18.5 molecular cloud. The structure of this map is consistent with instrumental noise, which is predominantly Gaussian (the stripes are associated with regions with a higher noise due to a lower integration time per pixel – see text for details). In Table 1, we show the pixel-to-pixel rms values calculated in the background annulus enclosed by the two concentric circles of this plot and in the dashed circle.

**Table 1.** rms pixel to pixel (pixel size 6.9 arcmin) calculated in the original maps, and in the average and difference divided by two of the two jackknife maps, in two different regions. The values above and below the horizontal line have been calculated, respectively, in the background annulus and in the dashed circle depicted in Fig. 3. The numbers in the last column correspond to the average noises in the original  $Q$  and  $U$  maps normalized by the integration time per pixel (units:  $\mu\text{K s}^{1/2}$ ).

$\nu$ (GHz)	$\sigma_I$ ( $\mu\text{K pixel}^{-1}$ )			$\sigma_Q$ ( $\mu\text{K pixel}^{-1}$ )			$\sigma_U$ ( $\mu\text{K pixel}^{-1}$ )			$\sigma_{Q,U}$ ( $\mu\text{K s}^{1/2}$ )
	Map	Sum	Diff.	Map	Sum	Diff.	Map	Sum	Diff.	
11.2	1592	1593	1277	389	396	394	361	361	361	1478
12.9	1328	1377	1119	300	308	314	293	301	297	1179
16.7	861	861	755	167	169	171	166	166	161	1158
18.7	1040	1041	966	199	202	213	201	205	201	1461
11.2	1377	1415	1320	406	418	460	315	335	346	1283
12.9	1331	1512	1529	352	387	349	309	339	351	1192
16.7	672	673	651	142	142	140	125	125	136	1009
18.7	803	809	876	149	150	157	164	165	163	1413

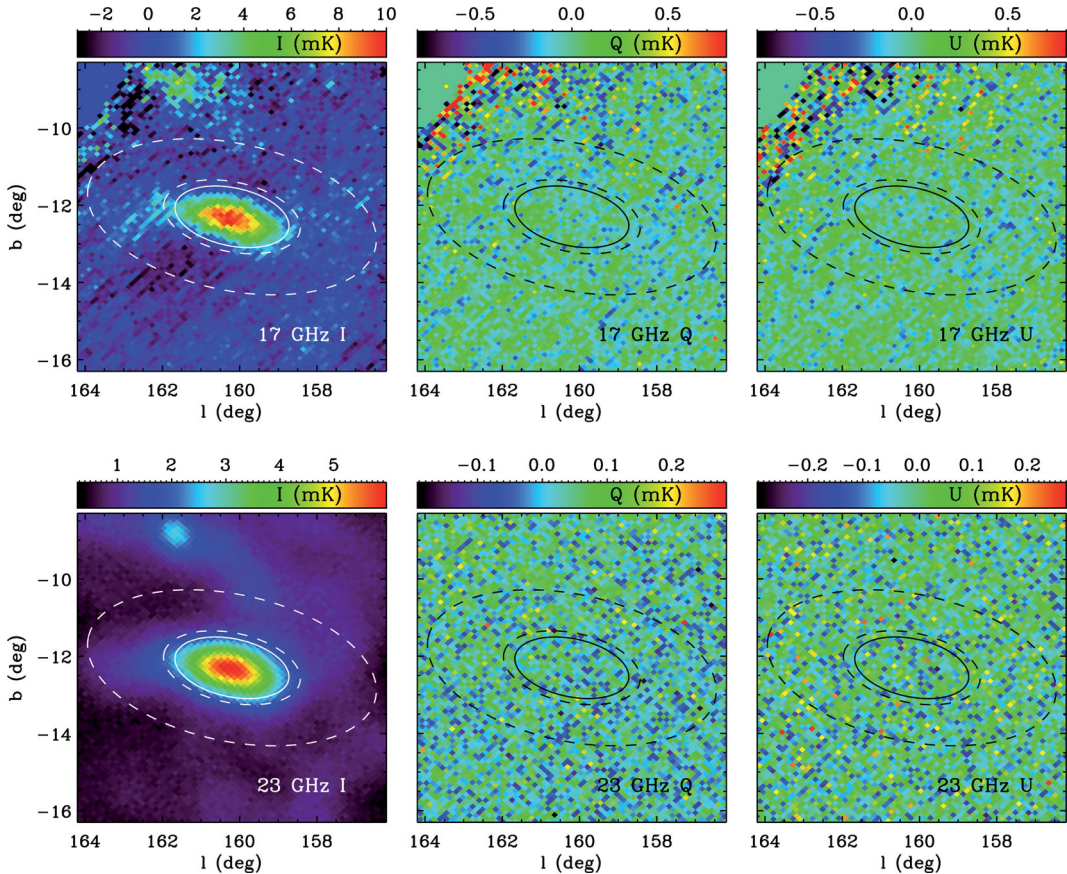


**Figure 4.** Intensity and polarisation maps around the California H II region, at 17 GHz from QUIJOTE and at 23 GHz from WMAP 9 yr data. The Stokes  $Q$  and  $U$  maps show zero polarisation as is expected for a free-free dominated region. This test therefore demonstrates the absence of significant polarisation systematics inherent to our experiment or to the data processing. The ellipses show the aperture and the background annulus that we use to derive polarisation upper limits in this region.

### 3.2 Intensity SED

As was indicated in Section 2.2, we take the COSMOSMAS flux densities for G159.6–18.5 from Planck Collaboration XX (2011), which have already been corrected for the flux loss caused by the filtering of COSMOSMAS data. While here we will use aperture photometry to derive our flux densities, in Planck Collaboration XX (2011) they were obtained by fitting the amplitude of an elliptical Gaussian with a fixed size of  $1.6^\circ \times 1.0^\circ$  (FWHM). In a first-order approximation, the flux densities obtained through Gaussian fitting will be equivalent to those obtained from aperture photometry using a given aperture size. Therefore, in order to get a reliable total intensity SED we choose a size for the aperture that gives the most similar flux densities to those presented in Planck Collaboration XX (2011) for the Haslam et al. (1982), Berkhuijsen (1972), Reich & Reich (1986), WMAP, Planck and DIRBE maps (it must be noted that the WMAP and Planck maps used in this work correspond to a different release to that used in Planck Collaboration XX (2011), but this will have a negligible effect). After trying different values, we found that a radius of  $1.7^\circ$  gives the best agreement, with a very low reduced chi-squared of  $\chi^2/\text{dof} = 0.098$ . The median of the background is computed in an external ring between  $1.7^\circ$  and  $1.7\sqrt{2}^\circ$ , which has the same area as the aperture. The derived flux densities in the QUIJOTE maps and in the other ancillary maps are listed in Table 2.

The final SED is depicted in Fig. 5, where the presence of AME clearly shows up at intermediate frequencies as an excess of emis-

sion over the other components. The intensities derived from these QUIJOTE observations trace, for the first time after the original measurements of the COSMOSMAS experiment (Watson et al. 2005), the downturn of the spectrum at frequencies below  $\sim 20$  GHz, as predicted by spinning dust models. In total, 13 data points are dominated by AME: the four QUIJOTE points, the four COSMOSMAS points, the WMAP 22.8, 33.0 and 40.7 GHz frequencies and the Planck 28.4 and 44.1 GHz frequencies. We perform a joint multicomponent fit to all the data, consisting of free-free emission, which dominates in the low-frequency tail, spinning dust, which dominates the intermediate frequencies, a CMB component, and thermal dust, which dominates the high-frequency end. As it was done in Planck Collaboration XX (2011), to avoid possible CO residuals we exclude from the fit the 100 and the 217 GHz values. We fix the spectrum of the free-free using the standard formulae shown in Planck Collaboration XX (2011), with a value for the electron temperature typical of the solar neighbourhood,  $T_e = 8000$  K, and fit for its amplitude, which is parametrized through the emission measure (EM).

Following Planck Collaboration XX (2011), we consider a high-density molecular phase and a low-density atomic phase which produce spinning dust emission, and fit their respective amplitudes, which are given by the hydrogen column densities  $N_H^{\text{mol}}$  and  $N_H^{\text{at}}$ . The CMB amplitude is denoted by  $\Delta T_{\text{cmb}}$ , and would correspond to the average of the primordial CMB fluctuations in the aperture. Finally, the thermal dust is modelled as a single-component modified blackbody curve,  $\tau_{250}(v/1200 \text{ GHz})^{\beta_d} B_v(T_d)$ , which depends

**Table 2.** Flux densities for G159.6-18.5 in the Perseus molecular cloud. They have been calculated through aperture photometry in a ring of radius  $1^{\circ}7$  and subtracting the median of the background in a ring between  $1^{\circ}7$  and  $1^{\circ}7\sqrt{2}$ , except those coming from the COSMOSMAS experiment (10.9, 12.7, 14.7 and 16.3 GHz), which have been taken from Planck Collaboration XX (2011). Also shown are the residual AME flux densities, obtained after subtraction of the free-free, CMB and thermal dust components. The last column indicate the telescope or survey from which the data have been extracted.

Frequency (GHz)	Flux density (Jy)	Flux density residual (Jy)	Telescope/survey
0.408	$10.5 \pm 4.0$	$2.7 \pm 4.2$	Haslam
0.82	$7.4 \pm 2.1$	$0.1 \pm 2.4$	Dwingeloo
1.42	$6.8 \pm 1.6$	$-0.1 \pm 2.0$	Reich
10.9	$16.1 \pm 1.8$	$10.3 \pm 1.9$	COSMO.
11.2	$15.0 \pm 2.0$	$9.2 \pm 2.1$	QUIJOTE
12.7	$20.0 \pm 2.2$	$14.2 \pm 2.2$	COSMO.
12.9	$18.1 \pm 2.1$	$12.4 \pm 2.1$	QUIJOTE
14.7	$28.4 \pm 3.1$	$22.6 \pm 3.1$	COSMO.
16.3	$35.8 \pm 4.0$	$30.0 \pm 4.0$	COSMO.
16.7	$33.9 \pm 2.4$	$28.1 \pm 2.5$	QUIJOTE
18.7	$35.2 \pm 3.7$	$29.2 \pm 3.8$	QUIJOTE
22.8	$40.2 \pm 2.4$	$34.0 \pm 2.5$	WMAP
28.4	$40.4 \pm 2.4$	$33.5 \pm 2.6$	Planck
33.0	$38.1 \pm 2.4$	$30.4 \pm 2.8$	WMAP
40.7	$32.8 \pm 2.5$	$23.1 \pm 3.3$	WMAP
44.1	$29.8 \pm 2.6$	$19.1 \pm 3.7$	Planck
60.8	$27.5 \pm 3.8$	$8.3 \pm 6.9$	WMAP
70.4	$32.3 \pm 4.9$	$5.2 \pm 10.0$	Planck
93.5	$59.5 \pm 9.3$	$1.8 \pm 22.3$	WMAP
100	$81 \pm 17$	$11 \pm 10$	Planck
143	$194 \pm 24$	$-17 \pm 82$	Planck
217	$1011 \pm 122$	$196 \pm 320$	Planck
353	$4286 \pm 446$	$344 \pm 1376$	Planck
545	$14858 \pm 1470$	$208 \pm 4588$	Planck
857	$45235 \pm 4045$	$-1352 \pm 13168$	Planck
1249	$86696 \pm 6674$	$-4878 \pm 25315$	DIRBE
2141	$114650 \pm 6891$	$6845 \pm 43590$	DIRBE
2998	$54361 \pm 2624$	$-837 \pm 28264$	DIRBE

on three parameters: the optical depth at  $250 \mu\text{m}$  ( $\tau_{250}$ ), the emissivity spectral index ( $\beta_d$ ) and the dust temperature ( $T_d$ ). Therefore, we jointly fit seven parameters to all the data points: EM,  $N_{\text{H}}^{\text{mol}}$ ,  $N_{\text{H}}^{\text{at}}$ ,  $\Delta T_{\text{cmb}}$ ,  $\tau_{250}$ ,  $\beta_d$  and  $T_d$ .

To define the spinning dust spectra of the molecular and atomic phases, we use the SPDUST.2 code<sup>7</sup> (Ali-Haïmoud et al. 2009; Silsbee et al. 2011). Initially, we use the same values as in Planck Collaboration XX (2011) for the different parameters on which the spinning dust emissivity depends. This involves a modification of the code, as by default it uses  $a_{0,1} = 0.35 \text{ nm}$  and  $a_{0,2} = 3.0 \text{ nm}$  for the centroids of the two lognormal functions defining the dust grains size distributions, while the carbon abundance per hydrogen nucleus,  $b_C$ , is selected from any of the values in table 1 of Weingartner & Draine (2001). Following Planck Collaboration XX (2011), we use instead  $a_{0,1} = 0.58$  and  $a_{0,2} = 0.53 \text{ nm}$ , respectively, for the molecular and atomic phases, and  $b_C = 68 \text{ ppm}$ . Using these two models, we get a good fit to our full data set, with  $\chi^2/\text{dof} = 0.99$ , where the spinning dust component is clearly dominated by the molecular phase, as was found by Planck Collaboration XX (2011).

<sup>7</sup> <http://www.tapir.caltech.edu/~yacine/spdust/spdust.html>

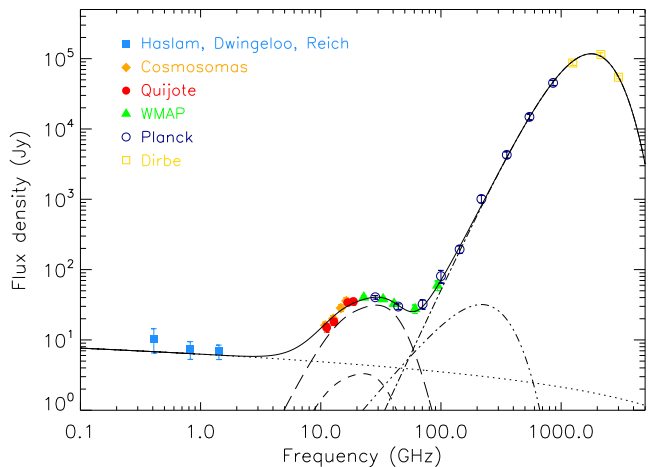


**Figure 5.** Spectral energy distribution of G159.6-18.5. QUIJOTE data points are depicted in red, together with other ancillary data including COSMOSMAS, WMAP 9 yr data and Planck data. At intermediate frequencies, the excess emission associated with the AME clearly shows up. A joint fit has been performed to all the data points except 100 and 217 GHz (which are affected by CO contamination), consisting of the following components: free-free (dotted line), spinning dust from a mixed environment with a high-density molecular (long-dashed line) and a low-density atomic (dashed line) gas, CMB (dashed-double-dotted line) and thermal dust (dash-dotted line). The solid line represents the sum of all the components.

To analyse the possibility of the existence of slightly different spinning dust models that could provide a better fit to the data, we take the AME residual flux densities from the previous fit, and produce a grid of models varying some of the parameters of the molecular phase component. In particular, we vary: (i) the hydrogen number density  $n_{\text{H}}$  between  $10$  and  $500 \text{ cm}^{-3}$  with a step of  $5 \text{ cm}^{-3}$ ; (ii) the kinetic gas temperature  $T_g$  between  $5$  and  $200 \text{ K}$  in steps of  $5 \text{ K}$ ; (iii) the intensity of the radiation field relative to the average interstellar radiation field, for which we consider only the values  $G_0 = 1$  and  $2$ ; (iv) and the hydrogen ionization fraction, for which we consider the values  $x_{\text{H}} = 10, 112, 1000$  and  $10000 \text{ ppm}$ . The best fit is obtained for  $G_0 = 1$  and  $x_{\text{H}} = 112 \text{ ppm}$ , the same values used in Planck Collaboration XX (2011). As the fit is very degenerate, to define the most-likely values for  $n_{\text{H}}$  and  $T_g$  we set Gaussian priors on four different parameters. First, we put soft priors on  $n_{\text{H}}$  and  $T_g$  centred on the same values used in Planck Collaboration XX (2011),  $(n_{\text{H}})_0 = 250 \text{ cm}^{-3}$  and  $(T_g)_0 = 40 \text{ K}$ , and with standard deviations  $\sigma(n_{\text{H}}) = 80 \text{ cm}^{-3}$  and  $\sigma(T_g) = 60 \text{ K}$ . These values are typical of the molecular cloud environment, which is known to be the dominant component to the spinning dust emission in G159.6-18.5 (Planck Collaboration XX 2011). For this medium Draine & Lazarian (1998) give values  $T_g = 20 \text{ K}$  and  $(n_{\text{H}})_0 = 300 \text{ cm}^{-3}$ , both inside the priors considered. An additional prior on  $N_{\text{H}}^{\text{mol}}$  can be derived from the canonical relation  $2.13 \times 10^{24} \text{ H cm}^{-2} = 1\tau_{100}$  (Finkbeiner, Langston & Minter 2004). Using  $\tau_{250}$  and  $\beta_d$  from our best-fitting model of the thermal dust component, we extrapolate the optical depth to  $100 \mu\text{m}$ , and find  $N_{\text{H}}^{\text{mol}} = 2.909 \times 10^{21} \text{ H cm}^{-2}$ . We use this value to define the centre of the Gaussian prior, and  $\sigma(N_{\text{H}}^{\text{mol}}) = 2 \times 10^{21} \text{ H cm}^{-2}$ . Finally, the ratio between the hydrogen column density and the hydrogen volume density,  $z = N_{\text{H}}^{\text{mol}}/n_{\text{H}}$ , gives an estimate of the length along the line of sight of the spinning-dust-emitting region. We assume that this length might be of the order of the transverse angular size of the source. The source subtends an angle of around  $2^\circ$ , which at the distance of the Perseus complex,  $260 \text{ pc}$  (Cernicharo, Bachiller & Duvert 1985), corresponds

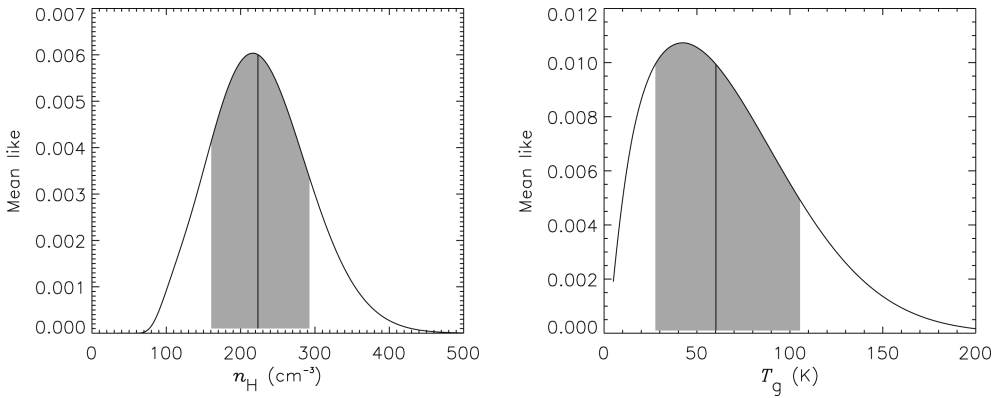


**Figure 6.** Likelihood distributions for the hydrogen number density (left) and for the kinetic gas temperature (right) associated with the molecular phase of the spinning dust component. These were obtained after marginalizing over the rest of parameters on which the spinning dust emissivity depends (see text for details). The vertical lines show the most-likely value, defined as the 50 per cent integral of the cumulative probability distribution, and the dashed regions depict the 68 per cent confidence interval around this value.

to 9.08 pc. We therefore set a fourth prior on this quantity defined by  $z_0 = 9.08$  pc and  $\sigma(z) = 4$  pc.

In Fig. 6, we show the marginalized likelihoods over  $n_{\text{H}}$  and  $T_g$ . We define the best values for these parameters from the 50 per cent integrals of the probability distribution, and the confidence intervals from the region encompassing the 68 per cent of the area around those values. We get  $n_{\text{H}} = 223.2^{+69.5}_{-62.8}$  and  $T_g = 60.2^{+45.3}_{-32.6}$  K. As mentioned above, the values of the intensity of the radiation field and of the hydrogen ionization fraction that maximize the likelihood are  $G_0 = 1$  and  $x_{\text{H}} = 112$  ppm, respectively. We fix the other parameters of the molecular phase, and all the parameters corresponding to the atomic phase, to the same values that were used in Planck Collaboration XX (2011). All these values are shown in Table 3. In this table,  $x_{\text{C}}$  represents the ionized carbon fractional abundance,  $y$  the molecular hydrogen fractional abundance and  $\beta$  the average dipole moment per atom. The meaning of the other parameters have been explained before in the text. We then obtain the corresponding spinning dust spectra for the molecular and atomic phases using these parameters as inputs for SPDUST.2. Fixing these spectra, we perform a joint fit of the five aforementioned components, obtaining the best-fitting values for the seven parameters defining these models, which are also shown in Table 3. We get  $\chi^2/\text{dof} = 0.99$ , the same value as before, so we do not manage to improve the quality of the global fit after improving the spinning dust models. This highlights the difficulty of constraining the parameters on which the spinning dust emission depends due to the strong degeneracies between them.

The total hydrogen column density is  $(4.40 \pm 0.83) \times 10^{21} \text{ H cm}^{-2}$ . This is a bit higher than the expected value of  $2.89 \times 10^{21} \text{ H cm}^{-2}$ , which has been derived from the aforementioned  $\tau_{100}-N_{\text{H}}$  canonical relation, and extrapolating  $\tau_{100}$  to  $\tau_{250}$  using the fitted spectrum for the thermal dust emission. The inferred lengths of the two spinning dust phases along the line of sight,  $z = N_{\text{H}}/n_{\text{H}}$ , are, respectively,  $z^{\text{mol}} = 5.63 \pm 0.76$  pc and  $z^{\text{at}} < 12.6$  pc (a 68.3 per cent C.L. upper bound is used here, as the error bar is higher than the estimate). These values are of the order, or compatible, with the transverse size of the region, 9.08 pc. Our fitted values for  $\beta_d$  and  $T_d$  are consistent within  $1\sigma$  with those derived in Planck Collaboration XX (2011). On the other hand, we get lower values for EM,  $N_{\text{H}}$  and  $\tau_{250}$ , but this is because these depend on the solid angle subtended by the region. This value is a factor  $\approx 5$  higher in our

**Table 3.** Model parameters. The emission measure EM is fitted to the data and defines the amplitude of the free-free emission. The following parameters are used as inputs for SPDUST.2, and define the shape of the spinning dust spectra for the molecular and atomic phases:  $n_{\text{H}}$  (hydrogen number density),  $G_0$  (intensity of the radiation field),  $T_g$  (kinetic gas temperature),  $x_{\text{H}}, x_{\text{C}}$  (hydrogen and carbon ionization fractions),  $y$  (molecular hydrogen abundance),  $a_{0,1}, a_{0,2}$  (parameters defining the dust grain distribution),  $b_{\text{C}}$  (carbon abundance per hydrogen nucleus) and  $\beta$  (average dipole moment per atom). The amplitude of these spectra are determined through the fit to the data, and are given by the hydrogen column density  $N_{\text{H}}$ . The best-fitting values for the amplitude of the CMB component  $\Delta T_{\text{cmb}}$  and for the three parameters defining the thermal dust spectrum ( $\beta_d, T_d, \tau_{250}$ ), as well as the reduced chi-squared, are also shown.

EM (\$\text{cm}^{-6} \text{ pc}\$)	$23.9 \pm 1.9$	
	Molecular	Atomic
$n_{\text{H}} (\text{cm}^{-3})$	223.2	30
$G_0$	1	2
$T_g (\text{K})$	60.2	100
$x_{\text{H}}$ (ppm)	112	410
$x_{\text{C}}$ (ppm)	1	100
$y$	1	0.1
$a_{0,1}$ (nm)	0.58	0.53
$a_{0,2}$ (nm)	3.0	3.0
$b_{\text{C}}$ (ppm)	68	68
$\beta$ (D)	9.34	9.34
$N_{\text{H}} (10^{21} \text{ cm}^{-2})$	$3.88 \pm 0.52$	$0.52 \pm 0.65$
$\Delta T_{\text{cmb}} (\mu\text{K})$	$22.6 \pm 13.6$	
$\beta_d$	$1.73 \pm 0.11$	
$T_d (\text{K})$	$18.2 \pm 0.6$	
$\tau_{250}$	$(2.78 \pm 0.41) \times 10^{-4}$	
$\chi^2/\text{dof}$	0.99	

case, because we are using aperture photometry instead of Gaussian fitting. When this factor is taken into account, then our values are brought into a better agreement with those of Planck Collaboration XX (2011). Finally, we find a positive value for  $\Delta T_{\text{cmb}}$ , whereas in Planck Collaboration XX (2011) it was negative. However, we have checked that our value agrees with the average level of the CMB anisotropies within the aperture, which has been found to be  $23.6 \mu\text{K}$ .

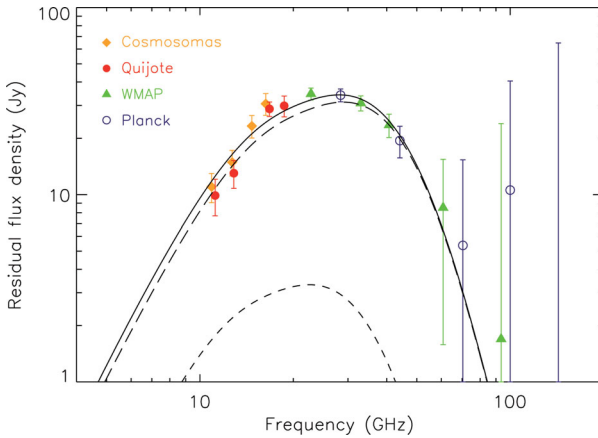


**Figure 7.** Spectrum of the AME in G159.6-18.5 after subtracting the best-fitting free-free, CMB and thermal dust components. The long-dashed line and the dashed line show, respectively, the spinning dust spectrum for the molecular and the atomic phases, while the solid line is the sum of the two.

in the *Planck*-DR1 CMB map resulting from the SMICA component separation method<sup>8</sup> (Planck Collaboration XII 2014c).

In Fig. 7, we show the residual spinning dust spectrum, obtained after subtracting the best-fitting free-free, CMB and thermal dust components.

### 3.3 Polarisation constraints

As no clear emission is seen in the  $Q$  and  $U$  maps of Fig. 2, we derive upper limits on the polarisation fraction of G159.6-18.5, following the procedure explained in Section 2.3. In Section 3.2, we defined the sizes of the aperture and of the background annulus so that we reproduced the flux densities in Planck Collaboration XX (2011), which were obtained through Gaussian fitting. In order to minimize the error associated with the background subtraction, here we extend the size of the background annulus, and use a circular aperture with radius  $1.5^\circ$ , and a background ring between  $1.5^\circ$  and  $2.5^\circ$ , with an extension towards the north-west as is shown in the maps of Fig. 2. At each frequency, we calculate the rms levels in this background annulus, to define the quantities  $\sigma(T_j)$  that are introduced in equation (5) to calculate the errors on the Stokes parameters  $Q$  and  $U$ . These errors, together with the flux densities resulting from the aperture photometry integration, are quoted in Table 4. Note that here the flux densities in total intensity in the QUIJOTE frequencies are slightly different to those presented in Table 2 owing to the different apertures. In order to get the AME residual values shown in Table 4, using the new flux densities we repeat the same fit that was performed in Section 3.2, considering the same spinning dust spectra for the molecular and atomic phases.

It is important to point out that, as it became clear when we discussed the results of the jackknife tests in Section 3.1, the uncertainties on the  $I$  flux densities are here biased high because some extended emission of the source leaks into the background annulus. This does not have significant implications in our analysis as the uncertainty in the polarisation fraction is driven by the errors in  $Q$  and  $U$ .

The  $Q$  and  $U$  flux densities shown in Table 4 are consistent with zero, and therefore we obtain de-biased (in Section 2.3 we explained

how this de-biasing is applied) upper limits at the 95 per cent confidence level on the polarized flux density,  $P_{\text{db}}$ . We also show in Table 4 upper limits at the 95 per cent confidence level on the polarisation fraction, taking as reference both the total ( $\Pi_{\text{db}}$ ) and the residual AME ( $\Pi_{\text{AME}, \text{db}}$ ) flux densities. The values below the horizontal line in this table correspond to constraints obtained in maps that have been built by combining the two frequency bands of each horn. The most stringent upper limit we get on the polarisation fraction is  $\Pi_{\text{db}} < 2.85$ ,  $\Pi_{\text{AME}, \text{db}} < 3.42$  per cent, and is obtained after combining the maps at 16.7 and 18.7 GHz. Due to the decrease of the flux density in total intensity at lower frequencies, the constraints at 11.2 and 12.9 GHz are less stringent.

Note that, under the reliable assumption that the free-free emission is unpolarized (Rybicki & Lightman 1979), any possible detection of polarisation at  $\nu \sim 10$ –30 GHz where, according to the total intensity SED shown in Section 3.2, the synchrotron and thermal dust emissions are clearly sub-dominant, should be ascribed to AME. One caveat to this hypothesis is the possible presence of a Faraday Screen (FS) hosting a strong and regular magnetic field, which could induce a rotation of the background polarized emission. This idea was proposed by Reich & Reich (2009) to explain the high degree of polarisation they detected towards G159.6-18.5 in observations from the Effelsberg telescope at 2.7 GHz. They suggest that this same mechanism could indeed be the responsible for the tentative polarized emission seen by Battistelli et al. (2006) at 11 GHz. Adopting the rotation measure obtained by Reich & Reich (2009),  $\text{RM} = 190 \text{ rad m}^{-2}$ , López-Caraballo et al. (2011) estimated a polarisation fraction of  $\lesssim 0.2$  per cent, well below the upper limit at this frequency. Using this RM, we estimate polarisation fractions from the FS of  $\approx 3.5$  and  $\approx 0.4$  per cent, respectively, at 11 and 19 GHz. These values are well below our upper limits, while the value at 11 GHz is compatible with the measurement of Battistelli et al. (2006).

In Section 3.1, we mentioned that one important consistency test for our data processing is the verification that it shows no polarisation at the position of unpolarized sources like the California H II region. In Table 5, we show the corresponding  $I$ ,  $Q$  and  $U$  flux densities, and derived upper limits on  $P$  and  $\Pi$ , which have been obtained using the apertures shown in Fig. 4. The limits on the polarisation fraction stand at the level of 2–4 per cent (95 per cent C.L.), depending on the frequency band. This constrains the possible existence of a leakage from intensity to polarisation to values below this level. In fact, as mentioned in Section 2.1, we expect the leakage to be below 0.3 per cent ( $\leq -25$  dB). This number has been verified using observations of Cas A, where we recover a leakage pattern with a quadrupolar shape in the  $Q$  and  $U$  maps, with a level of around 0.2 per cent (further details will be presented in separate technical papers).

We plot our constraints, and previous results in the literature at different frequencies, in Fig. 8. All the values correspond to the fractional polarisation with respect to the AME residual flux density,  $\Pi_{\text{AME}}$ . Battistelli et al. (2006) and López-Caraballo et al. (2011) give the polarisation fractions with respect to the total flux density,  $\Pi$ , so we inferred  $\Pi_{\text{AME}}$  by using a value for the ratio of AME to total flux density taken from our fitted SED in G159.6-18.5. It can be seen here that QUIJOTE observations fill the gap between previous results at frequencies below 11 and above 20 GHz. The point at 9.65 GHz is an upper limit coming from GBT observations on LDN1622 (Mason et al. 2009). The value at 11 GHz represents the aforementioned tentative detection towards G159.6-18.5 at the  $1.8\sigma$  level ( $\Pi = 3.4^{+1.5}_{-1.9}$  per cent, from which we get the depicted value of  $\Pi_{\text{AME}} = 5.3^{+2.5}_{-3.1}$  per cent) of AME polarisation from the

<sup>8</sup> Downloaded from the *Planck* Legacy Archive, [http://www.cosmops.esa.int/index.php?project=planck&page=Planck\\_Legacy\\_Archive](http://www.cosmops.esa.int/index.php?project=planck&page=Planck_Legacy_Archive).

**Table 4.** Intensity and polarisation flux densities at the position of G159.6-18.5 determined through an aperture photometry integration, and upper limits on the polarized flux density and on the polarisation fraction. We show the total intensity ( $I$ ) as well as the residual AME ( $I_{\text{AME}}$ ) flux densities after subtracting the free-free and thermal dust components. Similarly, for the polarisation fraction we show upper limits calculated with respect to the total and to the residual intensities. The error bars are at  $1\sigma$ , whereas the upper limits are given at the 95 per cent confidence level. Results are shown for each of the four QUIJOTE frequency channels, as well as for a combination of the low- and high-frequency bands.

$\nu$ (GHz)	$I$ (Jy)	$I_{\text{AME}}$ (Jy)	$Q$ (Jy)	$U$ (Jy)	$P_{\text{db}}$ (Jy)	$\Pi_{\text{db}}$ (per cent)	$\Pi_{\text{AME, db}}$ (per cent)
11.2	$14.0 \pm 3.3$	$9.4 \pm 3.4$	$-0.05 \pm 0.59$	$-0.39 \pm 0.47$	$<1.19$	$<8.79$	$<13.85$
12.9	$17.5 \pm 3.5$	$12.5 \pm 3.5$	$0.45 \pm 0.68$	$-0.23 \pm 0.56$	$<1.44$	$<8.46$	$<12.20$
16.7	$31.2 \pm 3.0$	$28.2 \pm 3.0$	$0.24 \pm 0.47$	$-0.83 \pm 0.52$	$<0.95$	$<5.14$	$<5.71$
18.7	$31.5 \pm 4.6$	$29.4 \pm 4.7$	$-0.11 \pm 0.75$	$0.18 \pm 0.70$	$<1.49$	$<4.76$	$<5.08$
12.0	$15.5 \pm 3.4$	$10.2 \pm 3.4$	$0.14 \pm 0.38$	$-0.36 \pm 0.37$	$<0.94$	$<6.26$	$<10.10$
17.7	$31.8 \pm 3.7$	$26.7 \pm 3.7$	$0.06 \pm 0.42$	$-0.26 \pm 0.40$	$<0.91$	$<2.85$	$<3.42$

**Table 5.** Intensity and polarisation flux densities of the California H II region determined through an aperture photometry integration, and upper limits on the polarized flux density and on the polarisation fraction. The error bars of  $I$ ,  $Q$  and  $U$  are at  $1\sigma$ , whereas the upper limits on the polarized flux density and on the polarisation fraction are referred to the 95 per cent confidence level.

$\nu$ (GHz)	$I$ (Jy)	$Q$ (Jy)	$U$ (Jy)	$P_{\text{db}}$ (Jy)	$\Pi_{\text{db}}$ (per cent)
11.2	$59.0 \pm 4.1$	$-0.45 \pm 0.36$	$0.52 \pm 0.42$	$<1.25$	$<2.12$
12.9	$54.7 \pm 4.2$	$-0.02 \pm 0.44$	$0.24 \pm 0.46$	$<0.96$	$<1.76$
16.7	$49.0 \pm 3.7$	$-0.07 \pm 0.38$	$0.38 \pm 0.35$	$<0.91$	$<1.87$
18.7	$51.8 \pm 6.2$	$-0.10 \pm 0.52$	$-0.68 \pm 0.50$	$<1.43$	$<2.82$

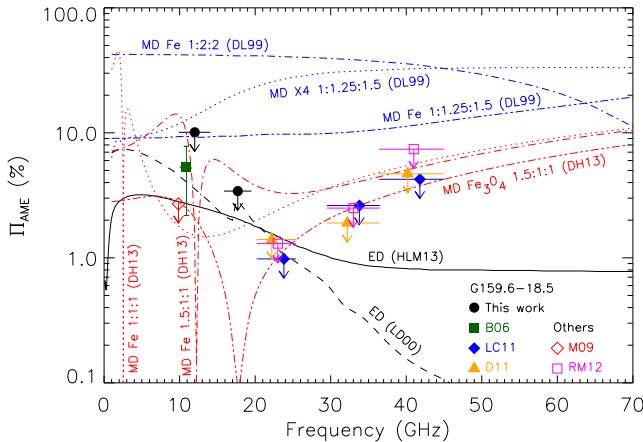


**Figure 8.** Constraints (95 percent C.L.) on several microwave emission models based on our upper limits on G159.6-18.5 (filled circles) and others in the literature on the same region (filled symbols; Battistelli et al. 2006; López-Caraballo et al. 2011; Dickinson et al. 2011), on LDN1622 (open diamond; Mason et al. 2009) and on [LPH96] 201.663+1.643 (open squares; Rubiño-Martín et al. 2012b). The horizontal lines around each data point represent the bandwidth of the corresponding detector. The black lines are theoretical predictions for the frequency dependence of the fractional polarisation of the electric dipole (ED) emission from Lazarian & Draine (2000, dashed line) and Hoang et al. (2013, solid line). The blue and red lines correspond, respectively, to the magnetic dipole (MD) emission models of Draine & Lazarian (1999) and Draine & Hensley (2013). Different grain compositions and geometries have been considered, as indicated by the label beside each line.

COSMOSMAS experiment (Battistelli et al. 2006). The points at  $\nu > 20$  GHz come from WMAP 7 yr data on the Perseus molecular cloud (López-Caraballo et al. 2011; Dickinson et al. 2011) and on the H II region [LPH96] 201.663+1.643 (Rubiño-Martín et al. 2012b), they also show less-stringent constraints from the Pleiades

reflection nebula and from the dark nebula LDN1622). Currently, the most stringent constraint is that obtained by López-Caraballo et al. (2011):  $\Pi_{\text{AME}} < 0.98$  per cent at 22.8 GHz. This limit benefits from the fact that it is obtained at a frequency close to the peak ( $\approx 28$  GHz) of the AME in G159.6-18.5. The constraints on the polarisation fraction from QUIJOTE come from a spectral region where the flux density in total intensity drops.

Together with the previously measured upper limits we show in Fig. 8 the theoretical predictions for the degree of polarisation of the spinning dust (Lazarian & Draine 2000, hereafter LD00; Hoang et al. 2013, hereafter HLM13) and of different models based on magnetic dipole emission (Draine & Lazarian 1999, hereafter DL99; Draine & Hensley 2013, hereafter DH13). The dashed line represents the prediction for the spinning dust polarisation for the case of a cold neutral medium from LD00, who assumed that grains are aligned via resonance paramagnetic relaxation. The solid line shows the polarisation degree estimated by HLM13, who inferred the alignment efficiency of interstellar dust grains from observations of the UV polarisation excess towards two stars. In so doing they assumed that the UV polarisation bump is produced exclusively by polycyclic aromatic hydrocarbon (PAH) molecules, those which are thought to be responsible for spinning dust emission. However, if the graphite grains were also aligned, contributing to the UV polarisation bump, then the alignment efficiency of PAHs could actually be lower and so would be the inferred degree of spinning dust polarisation. For this reason, this curve strictly represents an upper limit on the polarisation degree of the electric dipole emission.

In regard to the expected polarisation level of the magnetic dipole emission, we plot the DL99 models corresponding to dust grains ordered in a single magnetic domain. The different lines correspond to different grain shapes and compositions. In particular, we show the cases of grains made of metallic Fe, and of the hypothetical material X4 defined in DL99. For the grain geometries, different axial ratios  $a1:a2:a3$  are shown, as indicated in the figure. The models of DH13 include some improvements in the characterization of the

frequency dependence of the magnetic response, through the use of the Gilbert equation, with respect to [DL99](#). In their analysis, the magnetic particles are considered to be inclusions randomly oriented within the dust grains. In this case, the polarisation directions of the dipolar magnetic and electric emissions are expected to be orthogonal, and as a consequence the net polarisation fractions decrease with respect to the case of single-domain grains. We show in the figure polarisation degrees resulting from iron (Fe) and magnetite ( $\text{Fe}_3\text{O}_4$ ) inclusions with spherical and spheroidal shapes. The filling factors are  $f_{\text{fill}} = 0.15$  and  $f_{\text{fill}} = 0.3$ , respectively, for Fe and  $\text{Fe}_3\text{O}_4$  (see [DH13](#) for details).

As can be seen in Fig. 8, the electric dipole model of [LD00](#) appears to have been excluded by the upper limit at 9.85 GHz of [Mason et al. \(2009\)](#) on LDN1622 and by the one at 22.8 GHz from [López-Caraballo et al. \(2011\)](#). Since, as explained above, the prediction of [HLM13](#) must be regarded as an upper bound on the real polarisation degree, this model could yet be accommodated by the upper limit from [López-Caraballo et al. \(2011\)](#) if the graphite grains contribute to the observed UV polarisation. However, if the polarisation fraction were low enough to be consistent with this upper limit, the [HLM13](#) model would then be inconsistent with the tentative detection of [Battistelli et al. \(2006\)](#) at 11 GHz. The QUIJOTE observations at 12 and 18 GHz confirm the finding by other experiments at other frequencies, that the observed polarisation fraction is much less than that predicted by the [DL99](#) models of magnetic dipole emission which are based on grains with single ordered domains.

On the other hand, the two QUIJOTE points, and also the one from [Mason et al. \(2009\)](#), are compatible with the [DH13](#) model based on metallic Fe magnetic inclusions with spherical shape. However, this model, and the one corresponding to Fe spheroids are ruled out by higher frequency [WMAP](#) data. The latter of these models is also excluded by the [Mason et al. \(2009\)](#) and 18 GHz QUIJOTE upper limits. Among the different types of magnetic inclusions considered by [DH13](#), magnetite with spheroidal shape gives the lowest polarisation fractions. This case seems compatible with most of the observed data represented in Fig. 8, as it predicts polarisation degrees always below the observed constraints except for the case of the [WMAP](#) 33 GHz bound from [Dickinson et al. \(2011\)](#), which lies below.

It seems evident that observations at  $\sim 5$ –30 GHz might have the stronger discriminating power among magnetic dust models, as it is in this frequency range where the [DH13](#) models differ the most. Furthermore, at these frequencies the spinning dust polarisation fraction is expected to be higher (according to [HLM13](#) it peaks at 5 GHz), so a detection becomes potentially more likely. However, as it was pointed out above, at frequencies  $\lesssim 20$  GHz the drop of the AME flux density sets the requirement for more sensitivity on the polarized flux density. In the case of QUIJOTE, our upper limits on  $\Pi$  are not only affected by the decrease of the AME flux density at our frequencies, but also by the sparse sky coverage of our observations. We decided to survey an area large enough to cover the California H II region and also to get the source simultaneously in the four horns. Currently we are undertaking observations on a smaller area, centred in two individual horns, with the goal to increase by a factor  $\sim 10$  the integration time per unit area. This would improve our map sensitivity by a factor 3.2, helping to push our current upper limits on the AME polarisation fraction ( $\Pi_{\text{AME}}$ ) down to  $\approx 1.6$  per cent at 18.7 GHz, and  $\approx 1.1$  per cent after combining the 16.7 and 18.7 GHz frequency bands. This is well below the polarisation degree predicted by either of the spinning dust models of [LD00](#) or [HLM13](#) at these frequencies. Note in Fig. 8 that at

$\nu \gtrsim 30$  GHz these two models differ remarkably. Sensitive data at these frequencies may allow not only to probe the magnetic dust models but to distinguish between the [LD00](#) and [HLM13](#) models. The recently released *Planck* LFI polarisation data at 30 GHz, which is  $\approx 1.4$  more sensitive than [WMAP](#) 9 yr data in the Perseus region, may contribute in this regard. Future data from the TGI (at 30 GHz) and FGI (at 40 GHz) QUIJOTE instruments, which are nominally 13 and 11 times more sensitive than the current MFI, will push current [WMAP](#) upper limits by a significant amount. Taking the nominal TGI sensitivity as face value ([Rubíño-Martín et al. 2012a](#)), 100 h of data with this receiver on a  $6^\circ \times 6^\circ$  patch around G159.6–18.5 would allow to reach a sensitivity on  $\Pi_{\text{AME}}$  of  $\sim 0.1$  per cent, an order of magnitude better than current constraints.

## 4 CONCLUSIONS

We have presented the first results obtained with the QUIJOTE experiment, a new polarimeter aimed at measuring the B-mode anisotropy from inflation and also at characterizing the polarized foregrounds at low frequencies. These results are based on observations of the Perseus molecular complex, one of the regions where the AME has been extensively studied. Our observations cover G159.6–18.5, the region where AME is produced, and the California H II region. Our total intensity data on G159.6–18.5 trace the decrease of the flux density of this source at frequencies below  $\sim 20$  GHz, confirming the prediction of the models based on spinning dust radiation, which usually provide an excellent fit to the frequency spectrum of the AME. This confirms previous results on this region obtained with the COSMOSMAS experiment ([Watson et al. 2005](#)). When QUIJOTE measurements are combined with data coming from COSMOSMAS, [WMAP](#) 9 yr and *Planck*-DR1, we get a total intensity SED with 13 points between 10 and 50 GHz being dominated by AME, providing what probably is the most precise spectrum of this emission ever measured in an individual object. This total intensity SED is well fitted ( $\chi^2/\text{dof} = 0.99$ ) by a combination of free–free, CMB, thermal dust, and two spinning dust components associated to a high-density molecular phase and to a low-density atomic phase. We attempt to fit some of the parameters describing the physical environment of the cloud, and which define the shape of the spinning dust spectrum, but the solution is clearly degenerate and this approach does not achieve a better fit. However, after fixing the spinning dust spectra, we get plausible values for the seven parameters defining the five components of our model.

The California H II region is well detected in total intensity, presenting a spectrum at QUIJOTE frequencies consistent with free–free emission. The polarisation maps at the position of California are consistent with noise, as expected for regions dominated by free–free emission. No polarisation is detected at the position of G159.6–18.5 either, so then we extract upper limits on the polarized flux density and on its degree of polarisation. After combining the low-frequency and high-frequency maps of two horns of QUIJOTE, we get  $\Pi < 6.26$  per cent and  $\Pi < 2.85$  per cent (95 per cent C.L.), respectively, at 12.0 and 17.7 GHz. When these values are referred to the residual AME instead of to the total flux density, the limits are, respectively,  $\Pi_{\text{AME}} < 10.10$  and  $\Pi_{\text{AME}} < 3.42$  per cent. These constraints, which are the first obtained in the frequency range 12–20 GHz, confirm that the polarisation fractions towards regions with AME are lower than those predicted by single-domain magnetic dust models, but cannot yet distinguish between other models of the anomalous emission. Taking into consideration the data from other experiments at different frequencies, there is no single spinning

dust model that is consistent with all the derived constraints, while a magnetic dust model from spheroidal magnetite inclusions is compatible with most of the observed data. More sensitive data are necessary to push these upper limits or eventually to obtain a complete characterization of the level of AME polarisation. This would in turn help to disentangle between these different theoretical models, and also to assess up to what level AME will hinder the detection of the B-mode signal by current and future experiments operating in the frequency range 10–80 GHz. New QUIJOTE observations in G159.6-18.5 will increase the sensitivity of our maps, improving previous constraints at least by a factor of 2. This will allow us to reach a sensitivity on the polarisation fraction required to detect the levels predicted by electric dipole and some magnetic dipole emission models. However, given the similar levels of polarisation degrees predicted by the different models below 20 GHz, in order to discriminate between them we may need either an accurate characterization of the spectrum between 10 and 20 GHz, or eventually resort to the more sensitive data from *Planck* at  $\nu \gtrsim 30$  GHz or from the two future QUIJOTE instruments at 30 and 40 GHz, a frequency range where the electric and magnetic emissions present clearly different spectra.

## ACKNOWLEDGEMENTS

We thank Bruce Draine for providing the predicted polarisation degrees of the magnetic dipole emission models shown in Draine & Hensley (2013). This work has been partially funded by the Spanish Ministry of Economy and Competitiveness (MINECO) under the projects AYA2007-68058-C03-01, AYA2010-21766-C03-02, AYA2012-39475-C02-01 and the Consolider-Ingenio project CSD2010-00064 (EPI: Exploring the Physics of Inflation). CD acknowledges support from an ERC Starting (Consolidator) Grant (no. 307209), SH from an STFC-funded studentship, and CHLC from the DIULS (Research Directorship of the University of La Serena). We acknowledge the use of data from the *Planck*/ESA mission, downloaded from the Planck Legacy Archive, and of the Legacy Archive for Microwave Background Data Analysis (LAMBDA). Support for LAMBDA is provided by the NASA Office of Space Science. Some of the results in this paper have been derived using the HEALPIX (Górski et al. 2005) package.

## REFERENCES

- Ali-Haïmoud Y., Hirata C. M., Dickinson C., 2009, MNRAS, 395, 1055  
 AMI Consortium, Scaife A. M. M. et al., 2009, MNRAS, 400, 1394  
 Battistelli E. S., Rebolo R., Rubiño-Martín J. A., Hildebrandt S. R., Watson R. A., Gutiérrez C., Hoyland R. J., 2006, ApJ, 645, L141  
 Battistelli E. S. et al., 2015, ApJ, 801, 111  
 Bennett C. L. et al., 2013, ApJS, 208, 20  
 Berkhuijsen E. M., 1972, A&AS, 5, 263  
 Casassus S., Cabrera G. F., Förster Pearson T. J., Readhead A. C. S., Dickinson C., 2006, ApJ, 639, 951  
 Casassus S. et al., 2008, MNRAS, 391, 1075  
 Cernicharo J., Bachiller R., Duvert G., 1985, A&A, 149, 273  
 Davies R. D., Dickinson C., Banday A. J., Jaffe T. R., Górska K. M., Davis R. J., 2006, MNRAS, 370, 1125  
 de Oliveira-Costa A., Tegmark M., Page L. A., Boughn S. P., 1998, ApJ, 509, L9  
 de Oliveira-Costa A., Tegmark M., Gutierrez C. M., Jones A. W., Davies R. D., Lasenby A. N., Rebolo R., Watson R. A., 1999, ApJ, 527, L9  
 Dickinson C. et al., 2009, ApJ, 690, 1585  
 Dickinson C., Peel M., Vidal M., 2011, MNRAS, 418, L35  
 Draine B. T., Hensley B., 2013, ApJ, 765, 159 (DH13)  
 Draine B. T., Lazarian A., 1998, ApJ, 508, 157  
 Draine B. T., Lazarian A., 1999, ApJ, 512, 740 (DL99)  
 Finkbeiner D. P., Schlegel D. J., Frank C., Heiles C., 2002, ApJ, 566, 898  
 Finkbeiner D. P., Langston G. I., Minter A. H., 2004, ApJ, 617, 350  
 Génova-Santos R., Rebolo R., Rubiño-Martín J. A., López-Caraballo C. H., Hildebrandt S. R., 2011, ApJ, 743, 67  
 Górska K. M., Hivon E., Banday A. J., Wandelt B. D., Hansen F. K., Reinecke M., Bartelmann M., 2005, ApJ, 622, 759  
 Hafez Y. A. et al., 2008, MNRAS, 388, 1775  
 Haslam C. G. T., Salter C. J., Stoffel H., Wilson W. E., 1982, A&AS, 47, 1  
 Hauser M. G. et al., 1998, ApJ, 508, 25  
 Hoang T., Draine B. T., Lazarian A., 2010, ApJ, 715, 1462  
 Hoang T., Lazarian A., Martin P. G., 2013, ApJ, 779, 152 (HLM13)  
 Kamionkowski M., Kosowsky A., Stebbins A., 1997, Phys. Rev. D, 55, 7368  
 Kogut A., Banday A. J., Bennett C. L., Gorski K. M., Hinshaw G., Reach W. T., 1996a, ApJ, 460, 1  
 Kogut A., Banday A. J., Bennett C. L., Gorski K. M., Hinshaw G., Smoot G. F., Wright E. I., 1996b, ApJ, 464, L5  
 Lazarian A., Draine B. T., 2000, ApJ, 536, L15 (LD00)  
 Leitch E. M., Readhead A. C. S., Pearson T. J., Myers S. T., 1997, ApJ, 486, L23  
 López-Caraballo C. H., Rubiño-Martín J. A., Rebolo R., Génova-Santos R., 2011, ApJ, 729, 25  
 Macellari N., Pierpaoli E., Dickinson C., Vaillancourt J. E., 2011, MNRAS, 418, 888  
 Mason B. S., Robishaw T., Heiles C., Finkbeiner D., Dickinson C., 2009, ApJ, 697, 1187  
 Mather J. C., Fixsen D. J., Shafer R. A., Mosier C., Wilkinson D. T., 1999, ApJ, 512, 511  
 Murphy E. J. et al., 2010, ApJ, 709, L108  
 Planck Collaboration XX, 2011, A&A, 536, A20  
 Planck Collaboration XV, 2014a, A&A, 565, AA103  
 Planck Collaboration I, 2014b, A&A, 571, AA1  
 Planck Collaboration XII, 2014c, A&A, 571, AA12  
 Planck Collaboration XIII, 2014d, A&A, 571, AA13  
 Platania P., Burigana C., Maino D., Caserini E., Bersanelli M., Cappellini B., Mennella A., 2003, A&A, 410, 847  
 QUIET Collaboration, 2012, ApJ, 760, 145  
 Reich P., Reich W., 1986, A&AS, 63, 205  
 Reich W., Reich P., 2009, in Strassmeier K. G., Kovacichev A. G., Beckman J. E., eds, Proc. IAU Symp. 259, Cosmic Magnetic Fields: From Planets, to Stars and Galaxies. Cambridge Univ. Press, Cambridge, p. 603  
 Rubiño-Martín J. A. et al., 2012a, in Stepp L. M., Gilmozzi R., Hall H. J., eds, Proc. SPIE Conf. Ser., 8444, Ground-based and Airborne Telescopes IV. Amsterdam, Netherlands  
 Rubiño-Martín J. A., López-Caraballo C. H., Génova-Santos R., Rebolo R., 2012b, Adv. Astron., 8444, 351836  
 Rybicki G. B., Lightman A. P., 1979, Radiative Processes in Astrophysics. Wiley, New York  
 Silsbee K., Ali-Haïmoud Y., Hirata C. M., 2011, MNRAS, 411, 2750  
 Tibbs C. T. et al., 2010, MNRAS, 402, 1969  
 Tibbs C. T., Scaife A. M. M., Dickinson C., Paladini R., Davies R. D., Davis R. J., Grainge K. J. B., Watson R. A., 2013, ApJ, 768, 98  
 Vaillancourt J. E., 2006, PASP, 118, 1340  
 Vidal M. et al., 2011, MNRAS, 414, 2424  
 Watson R. A. et al., 2005, ApJ, 624, L89  
 Weiland J. L. et al., 2011, ApJS, 192, 19  
 Weingartner J. C., Draine B. T., 2001, ApJ, 548, 296  
 Ysard N., Verstraete L., 2010, A&A, 509, AA12  
 Zaldarriaga M., Seljak U., 1997, Phys. Rev. D, 55, 1830